Quantum Electronics **33** (7) 593 – 608 (2003)

PACS numbers: 52.38.-r; 62.50.+p
DOI: 10.1070/QE2003v033n07ABEH002466

Investigation of thermophysical and mechanical properties of matter under extremal conditions

I.K. Krasyuk, P.P. Pashinin, A.Yu. Semenov, V.E. Fortov

***Abstract*. The main results of experimental studies performed during the last ten years at the General Physics Institute, the Russian Academy of Sciences, on the properties of matter under extremal conditions created with the help of high-power laser radiation are presented. The problems associated with temperature measurements of the material behind the shock-wave front are discussed. The results of experimental studies of the mechanical properties of matter under conditions of ultrahigh deformation rates are presented. Examples of efficient application of numerical simulation for studying the mechanical and hydrodynamic processes occurring in matter subjected to high-power laser irradiation are given.**

Keywords: *laser radiation, shock wave, equation of state, pressure, temperature, deformation rate, spallation, numerical simulation.*

1. Introduction

During the last ten years, properties of matter under extremal conditions created with the help of high-power laser radiation have been carried out at the General Physics Institute (GPI), the Russian Academy of Sciences (see, for example, Refs [1 – 12]). These investigations were largely initiated by Academician A.M. Prokhorov, and were continued under his guidance and support. Apart from the staff of GPI, scientists from the Institute for High Energy Densities of the Joint Institute of High Temperatures, Russian Academy of Sciences, and from the Institute of Chemical Physics Problems, Russian Academy of Sciences, also participated in these studies.

Lasers offer a unique possibility of studying the physical properties of matter at high energy densities. For example, in experiments on laser-induced nuclear fusion, a significant compression of matter (1000 g cm^{-3}) or a considerable heating (100 keV) can be attained at the centre of shell-type spherical targets, depending on the type of targets and the conditions of irradiation. In the typical case of irradiation by a pulsed laser, absorption of energy by the target material leads to the formation of a high-temperature plasma. The hydrodynamic expansion of the plasma results in the emergence of an ablative pressure on the target caused by the recoil pulse. Under the action of this pulse, a shock wave with an amplitude of several hundred megabars is formed and starts propagating in the target. Heating and compression of the target material take place behind this wave front. The experimental methods developed at present make it possible to use such shock waves for obtaining the thermodynamic parameters of matter to derive the wide-range (over a wide range of variation of the parameters) semi-empirical equations of state. The application of lasers allows an investigation of the phase diagram regions that were not studied earlier.

Section 2 of this paper is devoted to the application of high-power laser shock waves for studying the thermophysical properties of matter under extremal conditions. Problems associated with the temperature measurements in the material behind the shock-wave front are discussed. One of these is the screening of optical radiation from the hot region by matter in the unloading wave. Another problem concerns the specific nature of the laser technique used for generating shock waves. Since a high-temperature plasma is formed at the front surface of the target, its radiation may cause a preheating of the target and, consequently, change its initial parameters.

In Section 3, another aspect connected with the application of laser shock waves, namely, the investigation of mechanical properties of matter at ultrahigh deformation rates, is presented. As a shock wave is reflected from the back surface of the target, a region of tensile stresses or 'negative' pressures is formed in the vicinity of the target. This leads to the phenomenon of spall, resulting in chipping of a part of the target material from the back surface. The use of laser shock waves also made it possible to study such phenomena at deformation rates for which the dynamic strength of the material approaches its theoretical limit.

Section 4 contains a review of the numerical methods used in Sections 2 and 3 for simulating the investigated shock-wave phenomena. Examples are given to demonstrate the efficient use of numerical simulation for studying the mechanical and hydrodynamic processes induced in matter by high-power laser radiation.

I.K. Krasyuk, P.P. Pashinin, A.Yu. Semenov A.M. Prokhorov General Physics Institute, Russian Academy of Sciences, ul. Vavilova 38, 119991 Moscow, Russia; e-mail: krasyuk@kapella.gpi.ru;
V.E. Fortov Institute for High Energy Densities, Joint Institute of High Temperatures, Russian Academy of Sciences, ul. Izhorskaya 13/19, 127412 Moscow, Russia

Received 29 January 2003
Kvantovaya Elektronika **33** (7) 593 – 608 (2003)
Translated by Ram Wadhwa

2. Thermophysical parameters of a dense plasma in a rarefaction wave

One of the main applications of laser shock waves is their use in the development of wide-range semiempirical equations of state for a substance [13]. The method of investigation is based on the use of algebraic relations between hydrodynamic values at the discontinuity surface, which are corollaries of the general laws of conservation of mass, momentum and energy for a one-dimensional steady-state motion [14]:

$$V = (D - U)V_0/D,$$
$$P = P_0 + DU/V_0, \quad (1)$$
$$E = E_0 + 0.5(P_0 + P)(V_0 - V).$$

Here, $V = 1/\rho$ is the specific volume, P is the pressure, E is the internal energy, D is the velocity of the shock-wave front moving in the unperturbed stationary matter, and U is the mass velocity, i.e., the velocity of particles behind the shock-wave front. Quantities with subscript '0' correspond to unperturbed matter ahead of the shock-wave front. Measuring any two of the five parameters (P, V, D, U and E) and using formulas (1), we can determine the hydrodynamic and thermodynamic parameters of the substance and establish a relation between them with the help of the caloric equation of state

$$E = E(P, V). \quad (2)$$

Usually, the kinematic parameters D and U are measured for metals. Measurements are made by recording the time in which the shock-wave front passes certain fixed (basic) distances. The accuracy of measurements of velocities D and U of the shock wave must not be worse than 5 % – 10 % in cases of practical importance.

The use of dynamic diagnostic techniques based on expression (1) for obtaining the shock adiabat assumes the stationarity and one-dimensionality of the flows of the substance under investigation. The stationarity and one-dimensionality are ensured by an appropriate choice of the target thickness and the diameter of the irradiation spot. Using the caloric equation of state (2), we can carry out hydrodynamic computation of the adiabatic flows of matter. However, to take into account the heat transport processes or the emission from a heated substance, the temperature should be specified explicitly as a function of pressure and volume:

$$T = T(P, V). \quad (3)$$

At present, for constructing total thermodynamic equations of state, an indirect method based on the solution of a linear homogeneous differential equation in T is used (see, for example, Ref. [15]),

$$\left[P + \left(\frac{\partial E}{\partial V}\right)_P\right]\frac{\partial T}{\partial P} - \left(\frac{\partial E}{\partial P}\right)_V\frac{\partial T}{\partial V} = T. \quad (4)$$

Equation (4) follows from the first law of thermodynamics and is supplemented by at least one experimentally obtained value of temperature as a boundary condition. The caloric equation of state (2) obtained for the region of the $P - V$ plane under consideration is used.

The interest towards direct temperature measurements in dynamic experiments stems from the fact that new data on temperature in various regions of the $P - V$ plane can help in refining the dependences $T = T(P, V)$, obtained by solving Eqn (4). Note that because of experimental problems and an ambiguity in the interpretation of the obtained results, only a small number of published works on laser shock-wave generation are devoted to direct measurements of the temperature of a substance behind the shock-wave front in metals.

In the case of metals, direct optical measurement of the temperature of the substance behind the shock-wave front is a quite complicated problem, mainly due to screening of radiation from hot regions of the target by the vapours of the substance in the unloading wave. The small duration of irradiation also complicates matters. It becomes necessary to satisfy a number of requirements to the design of the target and the accuracy of its preparation, to the quality and power of the laser beam, as well as to the space and time resolution of the recording instruments. For a typical laser pulse duration of ~ 1 ns, the target thickness should not exceed 15 – 20 μm, while the diameter of the irradiation spot should be at least 150 – 200 μm. The emerging experimental complications can be removed by using measuring instruments with a high spatial and temporal resolution, and by meeting certain requirements of precision of preparation and purity of the targets made from the material under investigation.

The initial state of the target is also very important because the laser generation of shock waves is associated with the formation of a high-temperature plasma at the front surface of the target; consequently, the target material can be preheated by the X-rays from the plasma corona and by a fast electron beam. This necessitates the development of suitable technique for measuring the temperature of preheating and for determining the initial state of the target material under investigation.

In this work, we discuss the possibility of using pyrometric technique for measuring the temperature of the target material behind the front of the shock wave emerging at the free surface of the target (Fig. 1). The experimental results [16 – 18] obtained by measuring the sample heating in the case of laser generation of shock waves in aluminium are compared with the results of numerical simulation. It is shown that preheating of the target can significantly affect the parameters of the optical signal detected from the back surface of the target, and hence the accuracy of measurements of temperature and pressure of the substance behind the shock-wave front.

2.1 Experimental conditions

The experimental setup is described in Ref. [16] and presented in Fig. 2. We used 0.53-μm laser radiation with an intensity up to 3×10^{14} W cm^{-2} at the target. The laser pulse of the FWHM duration 0.6 ns had a Gaussian shape. A special smoothing technique was used for obtaining a uniform distribution of intensity over a focal spot of diameter 200 μm [19]. Experiments were performed with step targets of aluminium prepared by using the sputtering technique. The choice of the target material was dictated by the fact that the equation of state for aluminium has been studied quite well (see, for example,

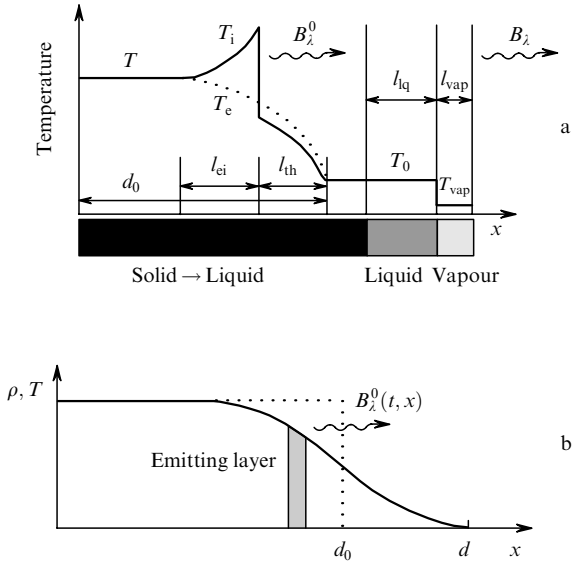

Figure 1. (a) Structure of the shock-wave front before emerging at the free target surface in the two-temperature approximation taking target preheating into account (T_i and T_e are the ion and electron temperatures, T_0 is the preheating temperature, T_{vap} is the temperature of the vapour of the material) and (b) schematic diagram of the spatial profiles of density ρ and temperature $T = T_i = T_e$ during effluence of the material in vacuum, i.e., during its unloading, after the emergence of a shock wave at the free surface. The dotted curve in Fig. 1b corresponds to the initial position of the back surface of the target ($x = d_0$).

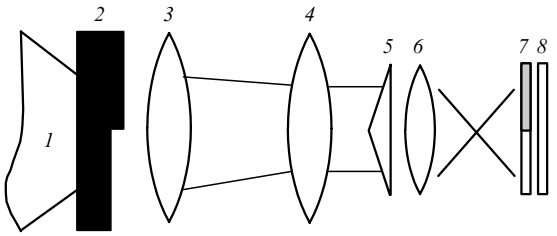

Figure 2. Schematic of the laser experiment [16]: (*1*) laser beam; (*2*) step target; (*3*, *4*, *6*) lenses; (*5*) biprism beamsplitter; (*7*) combination of 'red' and 'blue' optical filters; (*8*) input slit of the streak camera.

Refs [15, 20]). The thickness of the target base was 9.4 μm, and the step had a height of 4 μm for a transition zone width of about 2 μm (Fig. 2). The quality of target preparation was controlled with an electron microscope. The error in the measurement of the step height did not exceed 0.05 μm.

Radiation from the back side of the target was detected with a streak camera with a time resolution of 5 ps, equipped with a CCD array consisting of 12-bit elements (the total number of elements was 512 × 512). The quality of the shock wave was such that the time spread of the shock-wave front emerging at the back surface of a 13.8 μm-thick aluminium target did not exceed 5 ps within a spot of diameter 200 μm. As a whole, this spread characterises the quality of the target and the uniformity of its irradiation. The error in determining the shock-wave velocity under these conditions did not exceed 2.5 % for an absolute value of 24.5 km s^{-1}.

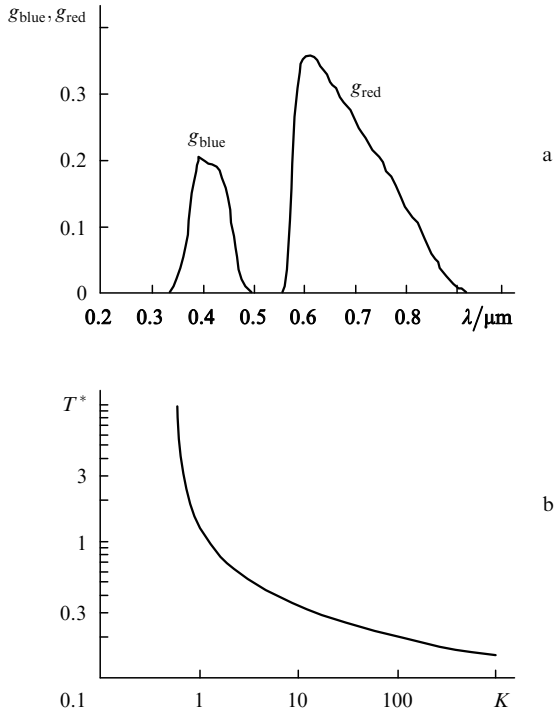

Figure 3. (a) Characteristics of a two-channel pyrometer: 'blue' and 'red' spectral sensitivities $g_{blue}(\lambda)$ and $g_{red}(\lambda)$ of the pyrometer channels and (b) the effective colour temperature calculated by using formula (7).

The colour temperature of matter in a rarefaction wave was measured with a two-channel pyrometer for recording the glow from the back surface of the target in the red (600 nm) and blue (400 nm) spectral regions. The optical system consisted of a biprism and two optical filters. Fig. 3a shows the characteristics of spectral transmission of each of the channels [16–18] taking into account the spectral sensitivity of the streak camera.

2.2 Numerical simulation

Numerical simulation technique was used for determining the shock-wave characteristics from the results of experimental measurements. One-dimensional time-dependent differential hydrodynamical equations of fluid dynamics expressing the laws of conservation of mass, momentum, and energy were solved numerically. The wide-range semi-empirical equation of state of the substance under investigation was taken into account [15].

A special computer programme (hydrodynamical numerical code) in Lagrangian variables [21] was developed to solve this problem. Section 4 of this paper is devoted to a detailed description of the numerical technique. The relation between ablation pressure pulse amplitude P_a and the laser radiation intensity I was described by the similarity relation [13]

$$P_a = A_p I^m, \tag{5}$$

where the coefficient A_p and the exponent m are determined by the specific conditions of laser irradiation [3].

We calculated the time dependence of the emission temperature of the substance in the rarefaction wave formed

after the emergence of a shock wave at the free (back) surface of the target (Fig. 1b) using the approach developed in Ref. [14] together with the above-mentioned hydrodynamical code for calculating the spatial density and temperature profiles of the matter at fixed successive instants of time during which the unloading wave existed (see Problem 4 in Section 4). In the course of the unloading of the target material, the radiation from the hot region is shielded by a layer of the colder substance (Fig. 1b). As a result, the detector receives radiation from the colder layers situated closer to the boundary of the expanding substance. The emitting layer is located at a distance from the boundary with the vacuum at which the optical thickness for the radiation being detected is approximately equal to unity. If we neglect the effect of thermal conductivity and radiation, the profiles of gas-dynamic parameters for a shock wave emerging at the free surface of the target, which are required for calculating the effective emission temperature, can be determined by solving the gas-dynamic Riemann problem. In this case, the solution lies on the isentrope of the unloading of the target material to vacuum.

Following Ref. [14], we consider the emission of a layer of the material with temperature and density distributions as shown in Fig. 1b. The spectral brightness of radiation on the free surface of the layer can be calculated from the expression [14]

$$B_\lambda = \int \mathrm{d}x B_\lambda^0(T(x,t))\tilde{\chi}_\lambda(x,t)\exp\left[-\int_0^x \tilde{\chi}_\lambda(\xi,t)\mathrm{d}\xi\right], \qquad (6)$$

where

$$B_\lambda^0 = \frac{2hc^2}{\lambda^5}\frac{1}{\exp[hc/(\lambda kT)]-1},$$

$$\tilde{\chi}_\lambda(x,t) = \chi_\lambda(x,t)\{1-\exp[-hc/(\lambda kT(x,t))]\}$$

are respectively the spectral brightness of thermal radiation and the absorption coefficient for optical radiation taking into account stimulated emission. The integral in (6) is calculated over the entire target thickness from its boundary with vacuum ($x = d$). The effective colour temperature T^* is determined from the relation

$$\frac{\int g_{\mathrm{red}} B_\lambda \mathrm{d}\lambda}{\int g_{\mathrm{blue}} B_\lambda \mathrm{d}\lambda} = K(T^*) = \frac{\int g_{\mathrm{red}} B_\lambda^0 \mathrm{d}\lambda}{\int g_{\mathrm{blue}} B_\lambda^0 \mathrm{d}\lambda}, \qquad (7)$$

where g_{red} and g_{blue} are respectively the red and blue spectral sensitivities of the pyrometer channels (Fig. 3a).

The plasma absorption coefficient was calculated by using a numerical code [22, 23] based on the generalised 'chemical' model taking into account the effects of imperfection, degeneracy, and metal-insulator transition. In this code, the absorption coefficient is calculated after determining the plasma composition by summing the contributions from all photoionisation channels, supplemented with the contribution of bremsstrahlung absorption in the field of ionised atoms.

Considerable difficulties are encountered while using expression (6) for calculations. This is due, first, to a very large range of variation in the absorption coefficient $\chi(x,t)$ (up to five orders of magnitude) and, second, to large gradients of $\chi(x,t)$ along the x axis. Because of these difficulties, integral (6) was calculated numerically using an irregular mesh with automatic condensation in the regions of large gradients and nonmonotonic behaviour of the integrands. The constructed algorithm is a combination of analytic formulas for exact integration and the methods of approximate representation of functions. Another approximation used for determining the absorption coefficient was the Kramers – Unsold formula derived for a singly ionised gas of hydrogen-like aluminium atoms [14]:

$$\frac{1}{\chi_\lambda} = \frac{1.2\times10^{-3}}{\lambda^3\rho T}\exp\left(\frac{5.99-1.24/\lambda}{T}\right). \qquad (8)$$

Here, χ_λ is measured in micrometers, λ is the radiation wavelength in micrometers, $\rho = \rho(x)$ and $T = T(x)$ are respectively the spatial distributions of density (in g cm^{-3}) and temperature (in electronvolts) in the emitting layer. The atomic weight of aluminium is 26.98 and the ionisation potential is 5.99 eV. The degree of ionisation was assumed unity in calculations.

2.3 Processing of experimental results

Figs 4 and 5 show the experimentally chronograms of emission in the red and blue spectral regions on the back surface of a step-shaped target [16]. To reduce the effect of statistical errors in subsequent data processing, the results of two experiments using similar parameters of laser irradiation of the target were combined. The least square method with a successive selection of nonlinear approximating functions was used for smoothing the emission curves. The results of smoothing are shown by thick curves in Figs 4 and 5. The approximating functions were chosen by taking into account the requirement of coincidence of the red and blue signal peaks, following from the properties of the blackbody radiation.

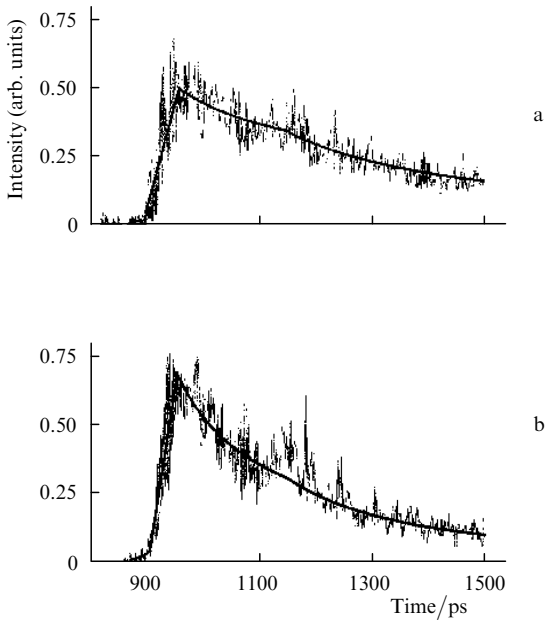

Figure 4. Optical signals recorded from the base surface of the target in the 'red' (a) and 'blue' (b) transmission bands of the pyrometer. The solid curves are the results of their smoothing. The intensities in both figures are presented in identical relative units.

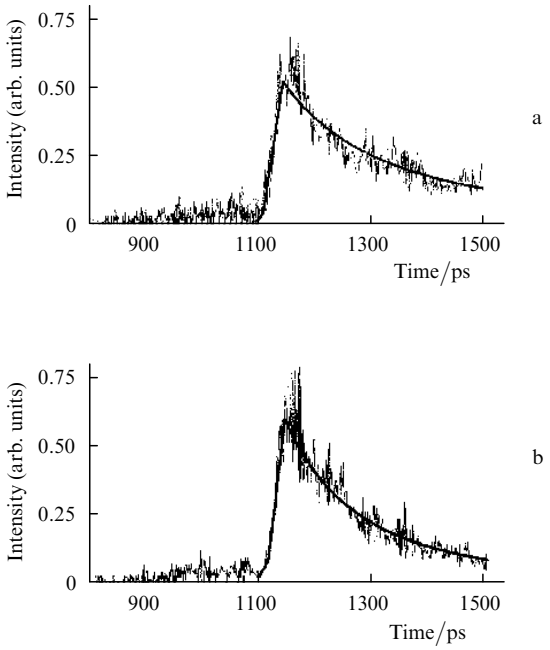

Figure 5. Optical signals recorded from the step of the target in the 'red' (a) and 'blue' (b) transmission bands of the pyrometer. The solid curves are the results of their smoothing. The intensities in both figures are presented in identical relative units.

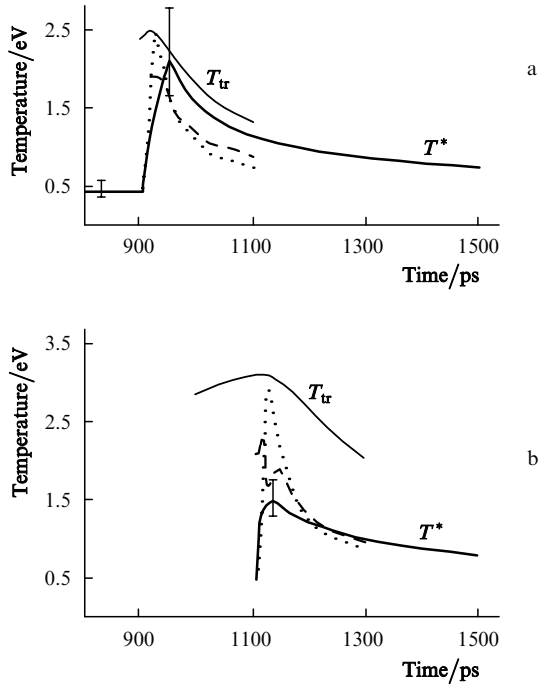

Figure 6. Temporal profile of temperature in a rarefaction wave at the emergence of a shock wave (a) at the base surface of the target and (b) at its step, computed using the total gasdynamic model and calculated from the experimental results. The bold solid curve is calculated value of the experimental colour temperature T^*, while the fine solid curve corresponds to the computed value of the maximum true temperature T_{tr}. The dotted curve shows the temperature calculated by using Eqns (6) and (7) and the semi-empirical model of optical density, while the dashed curve shows the temperature calculated by using Eqns (6) and (7) and the Kramers – Unsold formula for optical density.

The calculated dependence of the ratio of intensities of thermal radiation in the red and blue spectral regions on the blackbody temperature (Fig. 3b) was used for determining the temperature. This dependence was obtained by taking into account the spectral sensitivities g_{red} and g_{blue} of the channels shown in Fig. 3a. The thick curves in Fig. 6 show the results of calculation of the colour temperature of radiation at the base surface and the step of the target. A comparison of the temperature behaviour on both the surfaces of the target reveals the following. One can see that the maximum temperature at the step is lower than at the base surface of the target. Moreover, the durations of the fronts of temperature growth in these cases are also different (52.5 ps for the base surface and 33.5 ps for the step). In other words, the duration of the measured temperature growth front decreases with increasing thickness of the target. Note that the leading front of the curve obtained for the base surface shows traces of a pedestal indicating that the target was preheated to a temperature of $0.45^{+0.15}_{-0.06}$ eV.

2.4 Results of numerical simulation

2.4.1. Determination of the pressure pulse amplitude

The ablation pressure amplitude P_a on the front surface of the target was determined by comparing the measured time with the time obtained as a result of numerical simulation of the passage of the shock-wave front through a distance equal to the step height on the target. It was assumed that the pressure pulse repeats the shape of a laser pulse of the FWHM duration 0.6 ns.

A comparison of Figs 4a and 5a, as well as 4b and 5b shows that the delay of the emission signal from the step with respect to the signal from the base surface of the target is equal to 203 ps. This means that the shock-wave front propagates the distance $h_s = 4$ μm (step height) in a time $t_s = 203$ ps. Calculations show that the measured delay time t_s is related to the pressure amplitude $P_a = 6.8$ Mbar at the front surface of the target. Accordingly, the shock-wave pressure amplitude at the base distance inside the target (see Section 2.1) is $P_s = 6.5$ Mbar. On the other hand, if we assume that the shock-wave propagation in the case under consideration is stationary, the velocity of the shock-wave front can be calculated from the expression $D = h_s/t_s = 19.7\ \mathrm{km\,s^{-1}}$. Then, we obtain the pressure $P_{st} = 6$ Mbar behind the shock wave in the steady-state approximation from the shock adiabat table of aluminium for velocities [15, 20]. The difference in the pressures P_s and P_{st} indicates the attenuation of the shock wave during its propagation through the step and, consequently, to the approximate nature of the estimate obtained for the shock-wave amplitude in measurements of the average velocity of the shock-wave front.

2.4.2. Calculation of the temporal profile of the colour temperature

The spatial profiles of the density of the substance and its temperature in a rarefaction wave at preset instants of time close to the instants of time when the shock-wave front emerges at the free surfaces of the target (base surface and the surface of the step; see also Problem 4 in Section 4) were obtained by using the numerical hydrodynamical code supplemented with semiempirical wide-range thermodynamic complete real equation of state for aluminium.

Then the time dependences of the colour temperature at the base surface of the target and at its step (Fig. 6) were calculated using expressions (6) and (7) and the curve shown in Fig. 3b.

Various models used for determining the optical density of aluminium lead to close results, but the values obtained on the basis of the Kramers – Unsold model are slightly larger. Fig. 6 also shows the calculated temporal profiles of the maximum 'true' temperature $T_{tr}(t)$ of the substance in the unloading wave, which was determined as the maximum temperature in the theoretical temperature field for each instant of time.

A comparison of experimental and theoretical values of the temperature indicates a considerable shielding of the target region with the maximum temperature by a layer of the substance with a lower temperature, separating this region from the free surface of the target. The shielding is manifested more strongly at the step surface than at the base surface: the relative difference between the measured temperature and the maximum temperature at the base surface does not exceed 26 %, while the measured temperature in the rarefaction wave at the step surface is about half the maximum temperature. Moreover, equalisation of the measured temperature at the base surface with the calculated temperature occurs much more rapidly, viz., 55 ps after the emergence of the shock wave at the free surface. By way of comparison, it can be stated that the time after which these two quantities become equal at the surface of the step exceeds 400 ps. It will be shown below using the method of numerical simulation that the time of growth of the optical signals, and hence the duration of the rise front of the temperature being detected is influenced by preheating of the target (see Fig. 1a).

2.4.3. Effect of the shock-wave front structure on the duration of the optical signal rise front

Let us estimate the duration of rise in the emission signal from the back surface of a target as a function of the shock-wave front parameters. The finiteness of the spatial size l_f of the shock-wave front increases the duration $t_f = l_f/D$ of the front of the observed optical signal.

The schematic diagram of the shock-wave front structure [14] is shown in Fig. 1a. In a high-intensity shock wave, the ion temperature T_i differs sharply from the electron temperature T_e behind the shock wave, the ion temperature being much higher than the electron temperature. Because the intensity of optical radiation is mainly determined by the electron temperature, the rise in the optical signal being detected is determined by the rate of equalisation of the electron and ion temperatures.

Following Ref. [14], let us estimate the width of the relaxation zone $l_{ei} = t_{ei}D$ (t_{ei} is the electron – ion thermalisation time) over which the electron and ion temperatures are equalised. For a substance under normal conditions, the values of t_{ei} obtained by Spitzer [24] and by using the model taking plasma imperfection into account [25] are 15 and 0.2 fs, respectively. Hence, the relaxation zone width is $l_{ei} = 4 \times 10^{-6} - 3 \times 10^{-4}$ μm for $D = 20$ km s^{-1}.

The inclusion of the electron thermal conductivity leads to a thickness $l_{th} = (2/5)\varkappa/D = 2 \times 10^{-5} - 5 \times 10^{-3}$ μm of the preheating layer, $\varkappa$ being the electron thermal conductivity (see, for example, Ref. [14]). These estimates show that for a substance in the normal state ($T = 293$ K, $\rho = 2.7$ g cm^{-3}), the total width of the front before the shock-wave front cannot exceed $l_f = l_{ei} + l_{th} = 6 \times 10^{-3}$ μm, while the rise time $t_1^s = (l_{ei} + l_{th} + l_{opt})/D$ of the optical signal being detected must not exceed 1 ps. The quantity l_{opt} is the distance at which the signal emerges from the bulk of the substance and is detected by the detector. To be more precise, it is the thickness of the cold (unheated) layer of the substance near the back surface of the target with the optical thickness

$$\tau_{opt} = \int_{d-l_{opt}}^{d} \mathrm{d}x\chi(x) \approx 1\,,$$

where parameter d characterises the position of the target – vacuum interface (see Fig. 1b). Note that, since $l_{ei} \ll l_{th}$, the contribution from l_{ei} can be disregarded. For an aluminium target at room temperature, $l_{opt} \approx 10^{-2}$ μm.

The duration of the fronts of experimentally detected optical signals is found to be much larger than the theoretically estimated quantity t_1^s. The preheating of the target due to its effect on the shock-wave front duration and thermophysical parameters of the target may be one of the possible reasons behind the broadening of the fronts of these signals.

2.4.4. Effect of target preheating on the shock-wave parameters

We will present the results of numerical simulation of the emission of a substance on the free surface of a 9.4 μm-thick target taking its preheating into account. Calculations were made under the assumption that the target is heated due to a uniform heat release in the bulk of the sample with a constant (in time) power density 1.7×10^{13} W cm^{-3}. The substance may be preheated by X-rays or by a fast-electron beam from the plasma corona formed at the front surface of the target during laser generation of a shock wave whose intensity is assumed to be 2.3×10^{10} W cm^{-2}, i.e., about 0.1% of the laser radiation intensity. This assumption is consistent with the results of preheating of an aluminium target obtained in Ref. [26], and leads to the anticipated value 0.3 – 1 eV [27, 28] of preheating in the shock-wave front (see also Fig. 6a). The remaining conditions of the calculation corresponded to the experiment [16].

Note, however, for definiteness that for $I < 10^{14}$ W cm^{-2} under conditions of our experiments, the target is mainly preheated by X-rays rather than fast electrons, and such absorption is truly of an exponential type. The assumption about the homogeneity of the source of preheating is a simplification justified under the condition that the target thickness is smaller than the absorption length of X-rays.

First, the spatial density and temperature profiles were calculated taking into account the target preheating (Fig. 7). Then, the time variation of the colour temperature was calculated using relations (6) and (7) (Fig. 8b). The rise time t_2^s of the temperature calculated in this way is found to be equal to 22.5 ps, which is comparable with, but still smaller than the experimentally recorded value of 52.5 ps. Fig. 8a shows the durations of light signals as functions of the target thickness, which were recorded in Refs [16, 29, 30]. One can see that the rise times of light signals for X-ray method of generating shock waves exceed the values obtained upon direct laser irradiation on the target.

The above calculations show that, starting from instant $t_T = 0.5$ ns after the beginning of the process, metal expands isothermally in the vicinity of the surface at temperature

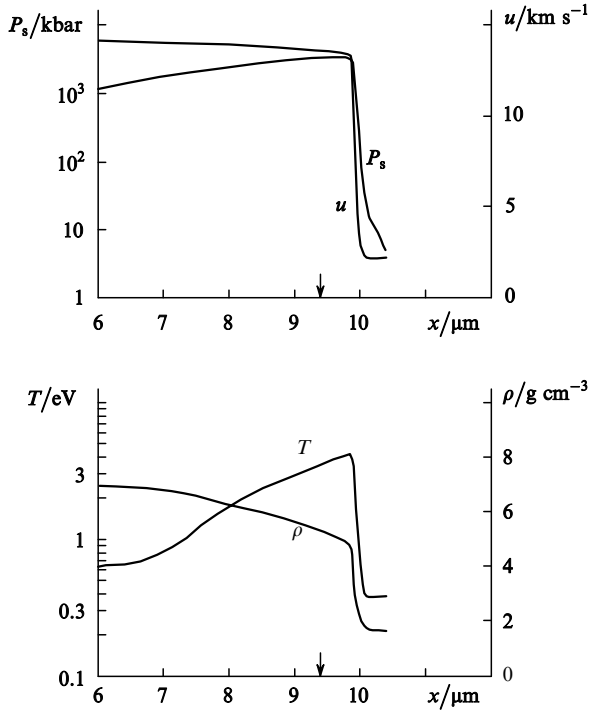

Figure 7. Spatial profiles of the parameters of a substance for a preheated target with surface temperature $T_0 = 5200$ K at the instant $t_b = 900$ ps corresponding to the emergence of the optical signal at the base surface of the target. Arrows show the initial position of the base surface of the target, and u is the velocity of matter in the target.

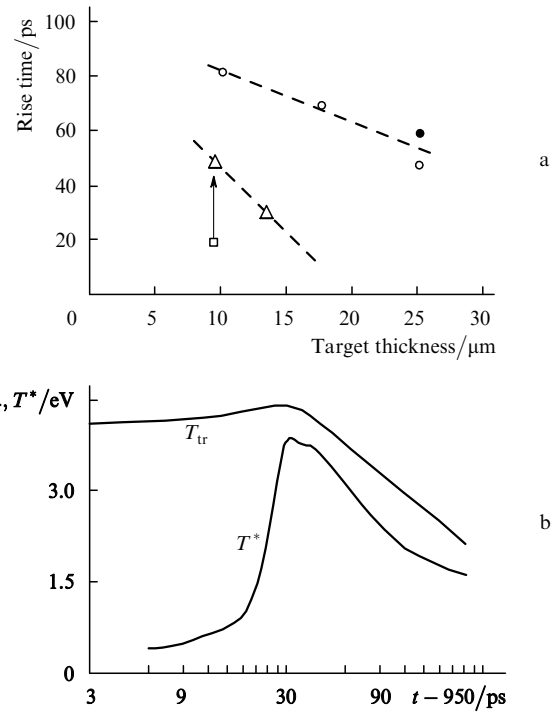

Figure 8. (a) Dependence of the duration of the experimentally recorded optical signal front on target thickness for shockwave generation by lasers (triangles, [16]) and X-rays (circles [29], bullets [30]), as well as the results of computations presented in Section 2.4.4 [squares – the arrow indicates the displacement of results taking into account the gaseous phase formation at the target surface (see Section 2.4.5)], and (b) computed temporal profiles of the colour ('observed') temperature T^* for a preheated target and the maximum 'true' temperature T_{tr} in a shock-compressed substance at the instant 950 ps corresponding to the maximum optical signal recorded from the base surface of the target (see Fig. 4).

$T_0 = 5200$ K $= 0.45$ eV. As a result of preheating, the expansion rate u_{exp} turns out to be equal to 2.2 km s^{-1}. Due to this expansion, the position of the shock wave is shifted to the right by approximately 1 μm by the moment of arrival of its front at the free surface of the target (see Fig. 7). The arrows in Fig. 7 show the initial position of the target – vacuum interface. The step height increases by $\delta h_s = u_{exp} t_s = 0.5$ μm, which indicates the change in the base distance by approximately 10 %. Thus, the preheating of the target, which changes the base distance, may considerably increase the error of experimental determination of the velocity of the shock-wave front. The substance in the rarefaction wave, passing through the solid and liquid states, enters the two-phase region (Fig. 9). In Fig. 1a, this region of states corresponds to T_0 and l_{lq}.

2.4.5. Calculation of the characteristics of the gaseous phase of the material at the liquid-vacuum interface

The limitations of the computer realisation of the numerical code did not allow a precise evaluation of the density of a substance in the gaseous phase. In Fig. 1, this region of states corresponds to T_{vap} and l_{vap}. Analytic estimates using the model of evaporation of a heated substance [31] were made in order to determine the characteristics of a substance in the gaseous phase. For an aluminium target, the atomic density n_0 of saturated vapour particles (in cm^{-3}) as a function of the surface temperature T_0 (in eV) is defined by the semiempirical relation [32]

$$n_0 = \frac{A}{T_0^{3/2}} \exp\left(-\frac{B}{T_0}\right), \qquad (9)$$

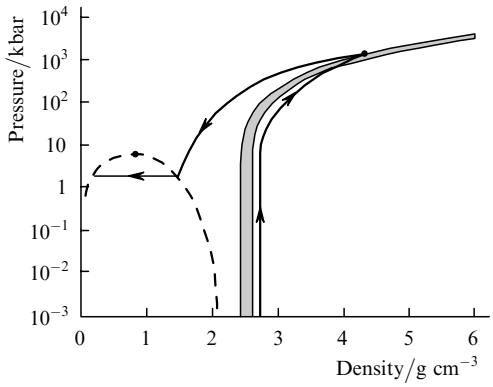

Figure 9. Phase diagram of aluminium [34]. The hatched region corresponds to the melting stage. The dashed curve is the liquid – vapour equilibrium curve. The trajectory marked by arrows indicates the change in state of the investigated substance as a result of preheating: compression, melting, isothermal expansion at $T_0 = 5200$ K, and getting into the unstable liquid – vapour region.

where $A = 2.47 \times 10^{23}$ and $B = 3.08$ (see [32]) are semiempirical coefficients. For $T_0 = 0.45$ eV, formula (9) gives $n_0 = 8.5 \times 10^{20}$ cm^{-3}. The gas-dynamic flux of the gas is formed at a distance $l = 1/(\sigma n_0) = 1.8 \times 10^{-6}$ cm, where $\sigma = 6.4 \times 10^{-16}$ cm^2 is the gas-dynamic cross section for aluminium atoms [32]. The density n of matter evaporated

in the hydrodynamical flow and its temperature T are connected with the saturated vapour density n_0 and the surface temperature T_0 through the relations [31]

$$n = 0.31n_0 = 2.6 \times 10^{20}\ \mathrm{cm}^{-3},\quad T = 0.65T_0 = 0.3\ \mathrm{eV}.$$

The gas-dynamic velocity u_{vap} of expansion of a cloud of vapour calculated by using formulas presented in Ref. [31] attains values up to 1.2 km s^{-1}. Since the effective time of vapour expansion $t_{\mathrm{vap}} = t_{\mathrm{b}} - t_T \approx 0.4$ ns (t_{b} =0.9 ns is the instant corresponding to the emergence of the optical signal at the base surface of the target and $t_T = 0.5$ ns marks the beginning of isothermal expansion), the vapour occupies a region of length $l_{\mathrm{vap}} = u_{\mathrm{vap}} t_{\mathrm{vap}} = 0.54$ μm. The optical thickness of this gaseous layer of aluminium is estimated as $\tau_{\mathrm{opt}} = 0.25$. The contribution of this layer to the total rise time of the optical signal is $t_3^{\mathrm{s}} = l_{\mathrm{vap}}/D = 27$ ps. Thus, according to the calculations made for the case of sample preheating, the total rise time $t^{\mathrm{s}} = t_1^{\mathrm{s}} + t_2^{\mathrm{s}} + t_3^{\mathrm{s}}$ for the observed optical signal is estimated at 50 ps, which coincides with the recorded value of 52.5 ps within the error limits.

Numerical calculations and analytic estimates show that, as a result of preheating, the free surface of the target acquires a layer of the substance of thickness ~ 1.5 μm in the liquid-gas mixed state, the density in this layer varying from 2.7 to 1.2×10^{-2} g cm^{-3}. In the phase diagram of aluminium (Fig. 9), the trajectory marked by arrows shows the change of state of the substance being investigated as a result of preheating. The layer of the substance formed on the free target surface in this case absorbs light, leading to a decrease in the optical signal amplitude and a distortion of the results of measurement of the 'true' temperature.

It follows from the above estimates that, while interpreting the results of experimental measurements of optical radiation, one must take into account the possibility of formation of a layer of the substance on the free target surface, the parameters of this layer differing from those for the initial state. The time required by the shock wave to cross this layer and the relaxation processes in the shock-wave front may considerably affect the rise time of the optical signal being detected. If this time is comparable with the time of expansion of the substance, shielding of radiation from the region with the highest temperature may lead to a considerable lowering of the observed temperature as compared to its real value.

Thus, while solving other problems in experiments on the application of laser generation of shock waves for studying the thermophysical properties of matter behind the shock-wave front, special attention should be paid to the evaluation of the parameters of the initial state of the target. In the first place, even a slight heating of the target can change its geometrical size; this, in turn, may significantly affect the accuracy of shock-wave measurements made under the assumption of a cold target. Second, preheating leads to the formation of a loose layer on the free target surface with sharply differing parameters. Relaxation processes in this layer may considerably distort the amplitude and shape of the optical signals from the free surface of the target used for determining the temperature of the substance in the unloading wave.

Experimental evaluation of the target preheating and steps aimed at its elimination continue to be a quite complicated problem. Because the emission brightness of the heated layer depends strongly on temperature, it is difficult to separate in a single experiment the optical signals from the preheated layer and the signals from the substance heated by a shock wave. It will be shown in this work that one of the ways for solving this problem is to estimate the target preheating from the rise time of the optical signal being recorded. For this purpose, the following experiment can be proposed. It is necessary to use a target consisting of two foils separated by a distance at which the one-dimensional nature of irradiation of the composite target is preserved (approximately 20–30 μm). The foil thicknesses are equal to the thickness of the base and the target step, chosen in our experiments on laser generation of shock waves. For a target of composite structure, a bright flash of light appears at the spot where the shock wave emerges at the back surface of the second foil with a delay of 1–1.5 ns. The sensitivity of the recording instrument can be improved significantly by lowering its time resolution.

The target preheating can be decreased by taking simple steps, e.g., by depositing on the front surface of the target a plastic ablator with a small atomic number Z and/or a layer of a substance for which the value of Z is much higher than the atomic number of the investigated target material. It was shown experimentally in Ref. [33] that the intensity of X-rays from the front surface of the target is lowered, thus leading to a decrease in preheating. In this case, a much better agreement is obtained between the measured and calculated parameters of the optical signal from the free surface of the target.

3. Mechanical properties of matter at high rates of deformation caused by a laser-induced shock wave

3.1 Experiment

Consider the results of investigation of the dynamic strength of an aluminium alloy for high deformation rates. For this purpose, we used the phenomenon of spallation associated with the reflection of a shock-wave front at the free surface of the target consisting of the substance under investigation [14] (Fig. 10). The shock wave in the target was generated by exposing its front surface to a laser pulse.

Experiments were carried out at the General Physics Institute using Kamerton and Sirius Nd : glass lasers. The main parameters of the lasers are: 'Kamerton' – radiation wavelength $\lambda = 0.53$ μm, maximum pulse energy $E_{\max} =$ 100 J, and pulse duration $t_{\mathrm{p}} = 2.5$ ns [35]; 'Sirius' – $\lambda =$ 1.06 μm, $E_{\max} = 60$ J, $t_{\mathrm{p}} =$ 5–80 ns, and pulse shape is triangular (see Ref. [36] for details). Fig. 11 shows the experimental setup schematically.

Laser radiation was focused on the target in a spot of diameter 1 mm. The target was a 180–460 μm-thick plate of AMg6M aluminium alloy consisting (see, for example, Ref. [32]) of aluminium with admixtures of Mn (0.3 %–0.6%) and Mg (5.5 %–6.5 %). The last letter in the abbreviation indicates that the alloy is annealed (soft), its density being 2.61 g cm^{-3} (slightly lower than the density 2.70 g cm^{-3} of aluminium). According to the results of numerical simulation (see Sec. 4.3), the edge effect was suppressed by preparing the targets with a 100-μm protrusion of diameter 1 mm on the back surface. In order to determine the instant t_{sp} of splitting in the experiments, a TDS-744A Tektronix oscilloscope was used to measure the

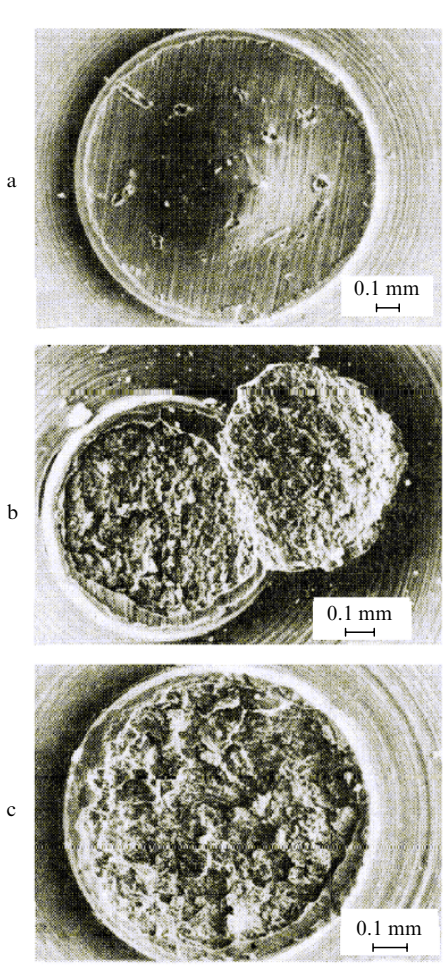

Figure 10. Results of interaction of a laser-induced shock wave with the target, leading to spall. As the ablative pressure increases, the front surface of the target shows (a) spall at the centre of a cylindrical step target (154 kbar); (b) its growth (187 kbar); and (c) its termination following a complete separation of the spall layer from the target (247 kbar). The experiments were carried out on the Sirius laser (General Physics Institute, RAS).

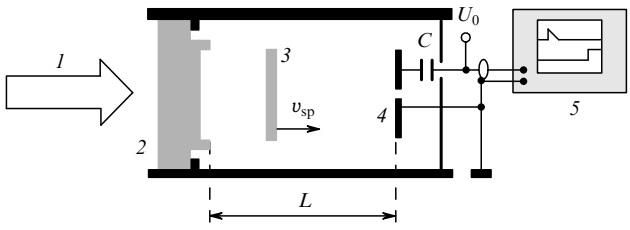

Figure 11. Experimental setup: (*1*) laser beam; (*2*) target; (*3*) spall layer; (*4*) electric-contact sensor; (*5*) oscilloscope; $C = 0.01$ μF, $U_0 = 10$ V.

time t_{arr} of arrival of the spall layer at the electric-contact sensor. The sensor was situated at a distance 110 – 880 μm from the target.

The spall strength and the time of separation of the spall layer from the target was determined by using the thickness h_{sp} of this layer and the time t_{arr} in each experiment. The peculiarities of the shock wave hardening of the material were studied in experiments with artificially spall layers. In this case, an aluminium foil of thickness 8 – 50 μm was gently pressed to the back surface of the target.

3.2 Simulation

Numerical simulation was used for calculating in each experiment the velocity of the layer separated from the target during the act of splitting. For this purpose, a one-dimensional nonstationary hydrodynamic code was worked out on the basis of the numerical solution of differential equations [21, 37, 38] expressing the laws of conservation of mass, momentum and energy, supplemented by the wide-range semi-empirical equation of state of the substance under investigation [15]. The AMg6M alloy was simulated by using the equation of state for aluminium in which the initial density ρ_0 was assumed to be equal to 2.61 g cm^{-3}. As in Sec. 2, the connection between the pressure pulse amplitude P_a and the laser radiation intensity I was established through the similarity relation (5).

3.3 Determination of the spall instant t_{sp}

In the part of the target left undamaged after the action of the shock wave, the mean position of the spall plane S and the average thickness of the spall layer h_{sp} were measured with the help of a microscope. The instant t_{sp} of spallation was determined by using the nonlinear equation

$$t_{sp} + L/v_{sp} = t_{arr}. \tag{10}$$

Here, L is the distance between the back side of the target and the electric-contact sensor. The velocity v_{sp} of the split layer was calculated with the help of numerical calculation of the pressure profile $P(t)$ in the spall plane S using the formula

$$v_{sp} = m_{sp}^{-1} \int_{t_0}^{t_{sp}} P(t)\mathrm{d}t, \tag{11}$$

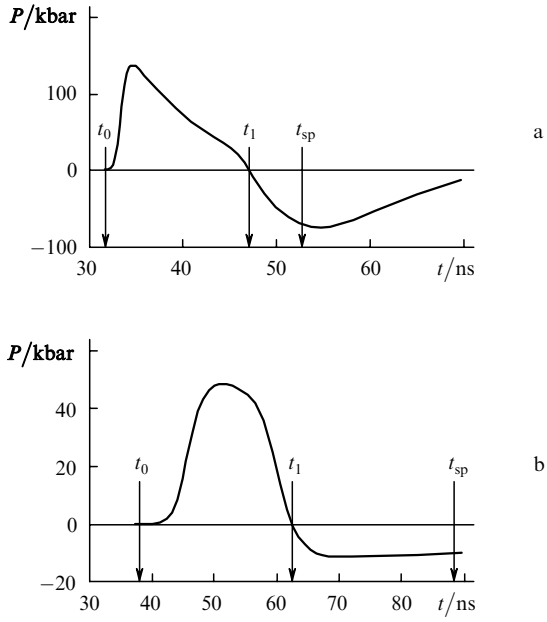

Figure 12. Pressure profiles in (a) dynamic and (b) quasistationary spallation modes.

where $m_{sp} = \rho_0 h_{sp}$ is the mass per unit surface area of the split layer. The instant t_0 corresponds to the beginning of the pressure pulse acting in the spall plane (Fig. 12). Then the spall strength σ^* of the material was calculated using the formula $\sigma^* = |P(t_{sp})|$. The strain rate of the material in the spall plane S at instant t_{sp}, which is defined by the formula $\dot{V}/V_0 = (dV/dt)/V_0 = -(d\rho/dt)/\rho_0$, was evaluated numerically.

Note that the fracture of the material is a complex kinetic process extended over a certain period of time [39]. For the sake of simplicity, it was assumed that the spallation occurs instantaneously after the attainment of a limit value of the negative pressure, corresponding to the dynamic strength of the material.

3.4 Experimental results

In our experiments, two main deformation modes leading to the fracture of the investigated material were observed. These modes, which can be termed as the dynamic mode and the quasistationary mode, differ qualitatively in that the load increases linearly in the first case right up to the instant of fracture, while in the second case the material is stretched rapidly, after which its fracture takes place under an almost constant load (see Fig. 12). The two mechanisms compete with each other, and the mode for which the spall occurs earlier under the given shock-wave loading conditions is the first to be realised.

3.4.1. Dynamic deformation mode

Fig. 13 shows the experimental dependence of the spall strength σ^* of the material on the strain rate $\dot{V}/V_0$. These data are supplemented with the earlier results of shock-wave experiments [40]. One can see that the dynamic spall strength of the material in this mode increases monotonically with the strain rate right up to 10^7 s^{-1} and can be described by the empirical relation

$$\sigma^* = 0.74(\dot{V}/V_0)^{2/9}, \tag{12}$$

where σ^* is measured in kilobars and $\dot{V}/V_0$ in inverse seconds. In the range $\dot{V}/V_0 = (1 - 1.5) \times 10^7$ s^{-1}, the dynamic splitting strength increases sharply to a value $\sigma^*_{dyn} =$ 80 kbar, after which it remains practically unchanged. This indicates the attainment of the limiting dynamic strength of the material under investigation. Its value has been estimated theoretically at ~ 100 kbar [40], which corresponds to the approximation of simultaneous fracture of all bonds in the solid.

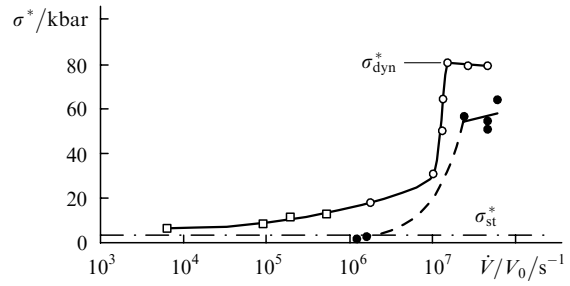

Figure 13. Dependence of the spall dynamic strength of the alloy AMg6M on the deformation rate for dynamic spall mode, obtained in laser (circles) and explosive (squares) experiments [40], as well as for an artificially spall layer (bullets). The solid curves are obtained by smoothing of experimental data using the least square method, while the dashed curves are the results of simulation.

As expected (see, for example, [41]), the results of experiments carried out using artificially spall layers (with the exception of two lower bullets in Fig. 13) show that the hardening of the material occurs in the contact plane between the artificial layer and the target surface. The static strength σ^*_{st} of the investigated material, measured in the limits $\dot{V}/V_0 \to 0$ and $t \to \infty$, is equal to 3.4 kbar [32] and is shown by the thin dot-and-dash line in Fig. 13.

3.4.2. Quasistationary deformation mode

At the initial stage of experiments, the material is deformed at a rate $\dot{V}/V_0$ exceeding 5×10^7 s^{-1}, after which it is in a stretched state over a time interval $\Delta t = t_{sp} - t_1$ under a practically constant load until fracture takes place (Fig. 12b). Here, t_1 is the instant at which the pressure becomes negative. Fig. 14 shows the experimental dependence of the spall strength on the duration of a quasistationary negative pressure pulse. Processing of the results of measurements by the least square method shows that the dynamic strength of the material in this case is almost inversely proportional to the duration Δt of the negative pressure pulse and satisfies the empirical relation

$$\sigma^* = 7 \times 10^2 \Delta t^{-5/4}, \tag{13}$$

where σ^* is measured in kilobars and Δt in nanoseconds.

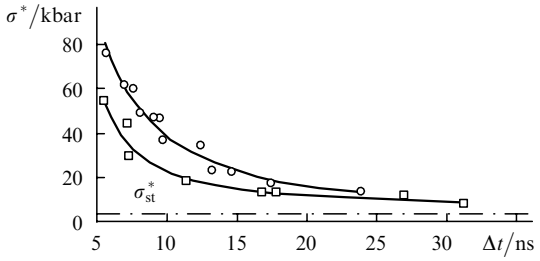

Figure 14. Dependence of the spall dynamic strength of the alloy AMg6M on the duration of tensile stress for the quasistationary spall mode, obtained in laser experiments (circles) and for an artificially spall layer (squares). The solid curves are obtained by smoothing of experimental data using the least square method.

For small Δt, the spall strength for the quasistationary mode tends to the limiting spall strength for the dynamic mode, attained for large values of $\dot{V}/V_0$. For $\Delta t \to 80$ ns, the spall strength tends to its static value of 3.4 kbar. The results of experiments made with artificially split layers (see Fig. 14) confirmed that the material is considerably hardened under the action of a shock wave in this case also.

Our experimental investigations have made it possible for the first time to determine the instant at which the spallation takes place. Dynamic strength studies in the aluminium alloy AMg6M showed that spall can take place for various types of nonstationary loading. These types can be classified as dynamic, quasistationary, and intermediate loading.

It is convenient to introduce the parameter $\xi = t_{sp}/t_m$ for systematising these modes (here, t_{sp} is the instant at which the tensile stress σ attains the value σ_{sp} corresponding to the beginning of spallation and t_m is the instant at which the

stress σ attains its maximum value. In this case, material is fractured upon a linear increase in the stress with time in the first mode (for $\xi \leqslant 1$). In the second mode ($\xi \geqslant 2$), rapid stretching and fracture of the material occur at a constant stress. The third mode ($1 < \xi < 2$) is a combination of stages with comparable durations of loading: at the first stage, the load increases linearly with time, while at the second stage it remains practically constant right up to the instant at which the layer is split from the target. The mode for which the sample is spalled earlier under the given conditions of shock-wave loading is actually realised in the experiment.

The ultimate dynamic load determined experimentally for the first time for the aluminium alloy AMg6M was found to be equal to 80 kbar, which is close to the theoretical estimate of 100 kbar.

4. Numerical simulation of shock-wave phenomena

Numerical simulation of physical processes has become an important component of scientific research. In many cases, the results of simulation provide new information on the internal nature of a process under investigation, whose characteristics cannot be measured by experimental methods as yet. In particular, such information gained from numerical calculations has made it possible to detect and give a physical interpretation to the spall mechanism described in Section 3, which was unknown earlier.

Simulation of phenomena and processes studied in some applied investigations and experiments necessitates further development and improvement of the methods leading to reliable numerical results. This is important, for example, for simulating the flow of media with arbitrary equations of states. Such problems include the simulation of high-intensity shock wave propagation in various media and high-velocity impacts in which certain real properties of a substance become significant. The efficiency of using numerical simulation or studying thermophysical and mechanical properties of a substance subjected to shock-wave action is demonstrated in Sections 2 and 3.

A large number of special programmes and algorithms have been developed to take into account the properties of a substance (i.e., its equation of state) for a wide range of thermodynamic parameters. In particular, these algorithms are used for determining the values of pressure, velocity of sound, and temperature using the values of density and internal energy. The results can be presented in the form of tables as well as analytic relations approximating the dependences of thermodynamic parameters of the substance. The application of such equations of states necessitates the adaptation of the existing numerical methods to such equation or the use of new methods specially developed for such equations of state.

4.1 Peculiarities of numerical simulation of shock-wave phenomena

Consider in greater detail the specific difficulties which have to be overcome in analysis of wide-range equations of state as applied to gas-dynamic equations describing the laws of conservation of mass, momentum, and energy (see, for example, [14, 37, 38]). At present, a number of quite reliable and widely used numerical methods have been developed for calculating the flows of media with model equations of state (in particular, for a perfect gas). However, the following particular problems are encountered during attempts to extend these models to the region of nonideal equations of state.

Consider first implicit discrete difference schemes used for approximating the initial partial differential equations. The application of implicit difference schemes consisting of nonlinear systems of algebraic equations for the required values of mesh functions involves difficulties associated with the convergence of iterative processes used for finding a solution. This can be attributed quite often to nonstandard behaviour of the equation of state in certain regions. Additional difficulties are encountered, for example, in Newton's iterative method since it requires the knowledge of the derivatives of thermodynamic parameters (which also complicates the equation of state) as well as the discontinuities of the derivatives themselves. The frequently used quasi-linearisation of the equations does not simplify matters since it cannot be employed in every situation and may also introduce uncontrollable errors.

The last remark also applies to the methods (both explicit and implicit) in which certain forms of artificial viscosity have to be taken into consideration. In particular, the frequently used Neumann – Richtmyer quadratic viscosity [42, 43], derived under the conditions of the equations of states of a perfect gas, may lead to serious errors when used improperly [44]. In a real wide-range equation of state, such errors may even increase in general. No reliable procedure has been worked out for controlling the introduced error.

The same applies to explicit as well as implicit numerical methods based on a meticulous preliminary multiparametric tuning of the numerical algorithm on the basis of certain principles. For example, such a situation arises during the correction of the flows [45, 46], where the numerical solution is specially modified using the properties of the exact solution of the nonlinear advection equation. The application of such methods sometimes raises questions concerning the propriety of a certain *a priori* tuning of the method to obtain a solution whose properties, strictly speaking, are not known beforehand. It appears that the numerical solution may become distorted in the case of some quite complicated interactions.

Such arguments necessitate the use of algorithms in gas-dynamic analysis with arbitrary equations of state, which would be most natural in a certain sense for the given system of equations without introducing any additional concepts that are not consequent of the specific nature of these equations of state. Such an approach permits the selection and application of only those methods, which are based directly on the properties of the gas-dynamic equations themselves. These include Godunov's method [47 – 49] and its hybrid modifications as well as other types of Godunov's method, e.g., Roe's method [50, 51], Courant – Isaacson – Rees method [52], and some other methods (see the literature cited in Refs [37, 38]). Here, hybrid modification indicates that the algorithm may change its properties, for example, the order of approximation. All these methods are explicit and provide the most adequate description of the vicinity of influence of gasdynamic system of equations.

Generally speaking, Godunov's method is nonlinear and is based on the exact solution of the problem of decay of an arbitrary gas-dynamic discontinuity (Riemann's problem). Roe's method is 'quasi-linear': a special explicit averaging procedure based on the solution preserving a number of properties of Godunov's method based on the exact solution

was used for calculating the mesh function at the boundary of mesh cells. Unfortunately, Roe's method can be used only under certain conditions imposed on the equation of state being used [37, 38]. The Courant – Isaacson – Rees method is 'linear' in a certain sense: Riemann invariants of a locally linearised system of hyperbolic-type equations are used to determine the mesh parameters at the boundaries of difference cells. An additional advantage of this method over the previous two methods is that it does not require the conservative forms of the initial system of equations. In particular, this allows the construction of a difference scheme, including one for a basically non-conservative system of equations of two-temperature gas dynamics. Quite arbitrary equations of state can be used in this method. When applied for numerical computations, the Courant – Isaacson – Rees method exhibited high reliability, efficiency, and simplicity over a wide range of interactions and for all the equations of state used in the analysis (see, for example, Refs [2, 21, 37, 38]).

A few words about the hybrid modification or the variable order of the numerical method are appropriate here. Hybridisation is introduced to ensure the second order of accuracy in the smooth regions of the solution without changing the algorithm of the through solution, and to carry out computations using a reliable algorithm with the first order of accuracy, having good smoothing properties in the region with strong gradients of the mesh functions. The introduction of the hybrid modification thus makes it possible to combine the positive properties of algorithms having the first order of accuracy (e.g., monotonicity and the absence of oscillations in the regions of large gradients) and the second order of accuracy (higher accuracy in the regions of smooth solution). In particular, the hybrid modification of the algorithms for gas-dynamics equations increases the accuracy of computation of contact discontinuities, rarefaction waves, etc., avoiding at the same time non-physical oscillations at the shock-wave fronts.

4.2 Results of numerical calculations of one-dimensional spallations

The numerical method developed by us was used to carry out a number of calculations for test problems, as well as one- and two-dimensional applied problems (see Refs [2, 21, 37, 38] for details).

Problem 1. Fig. 15 shows the numerical results of gas-dynamic simulation of shock wave propagation in an aluminium target, obtained in Lagrangian coordinates. Calculations were made by using the real equation of state of the target material, viz., aluminium. The following initial conditions were chosen. A 50-μm-thick aluminium target was exposed from the left (Fig. 15a) to a pressure pulse of trapezoidal shape having a total duration of 0.3 ns with rising and falling pressure regions of duration 0.03 and 0.01 ns respectively. The maximum amplitude of the pressure pulse was equal to 28 Mbar. Numerical simulation was carried out for a wide-range equation of state [15, 34, 53] used both in tabular form and as an analytic approximation in the form of a computer programme. The results of numerical simulation were compared with the results of computations [54] made by using the numerical code Lasnex (USA) and an equation of state of the type presented in [20].

Fig. 15a shows the pressure profiles in a shock wave at various instants of time following the onset of the pressure pulse. Curves (*1*), (*2*), (*3*) and (*4*) correspond to the

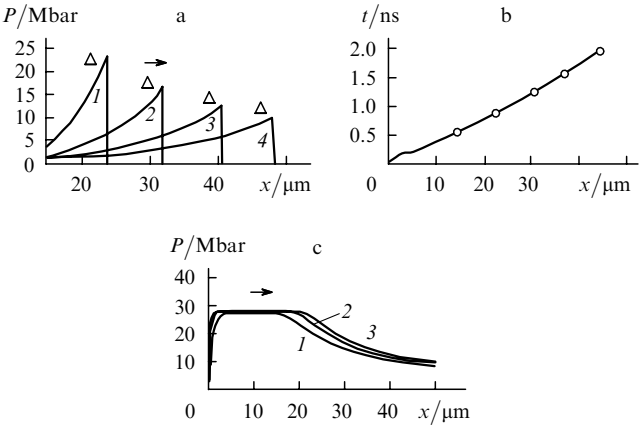

Figure 15. Simulation of shock wave propagation in a plane aluminium target. The arrows indicate the direction of propagation of the wave.

instants 0.65, 0.9, 1.2 and 1.5 ns respectively. The triangles over the curves show the maximum pressure values obtained by solving the same problem using the Lasnex code and the appropriate time instants. The slight disparity in the maximum pressures shown in Fig. 15a is due to different equations of state used in computations [20]. Fig. 15b shows the movement of the shock-wave front caused by the action of a pulse of the same trapezoidal form with a maximum pressure of 13 Mbar. The circles correspond to the results obtained in Ref. [54]. The velocity D of the shock-wave front relative to the gas at rest is connected in our case with the velocity U of matter behind the shock wave for aluminium through the semiempirical relation $D = 5.289 + 1.238U$ [15]. The coordinate dependence of the maximum pressure attained at a given point on the target during the entire period of intersection is shown in Fig. 15c. The reliability of the numerical computations was verified by checking the convergence. One can see that the numerical results converge for a spatial mesh width $\Delta x = 0.5$, 0.25 and 0.125 μm respectively for curves (*1*), (*2*), and (*3*).

In the calculations whose results are presented in Fig. 15, the Courant number C responsible for the stability of computations was assumed to be equal to 0.2. It should be recalled that the theoretical estimate of stability gives a value $C \leqslant 1$. The use of larger values of Courant numbers equal to 0.8 – 0.9 sometimes leads to non-physical values of thermodynamic variables, which were found to be lower than the values defined by 'cold' pressure curves for pressure and internal energy.

Calculations were made by using a wide-range semiempirical equation of state describing a solid, liquid, gas, plasma and a mixture of theses states [15]. This equation of state depends on about 50 parameters, most of which are fundamental constants of a substance, and 15 are chosen from the condition of best agreement between the experimental values of temperatures and densities at transition points, in particular the metal – insulator transition, on the phase diagrams. Numerical simulation was carried out for equations of state in two forms. The first form consists of tables showing the velocity of sound and pressure as functions of density and internal energy, which were stored in the memory of the computer. The second form includes the software used for calculating with the required accuracy the velocity of sound and pressure $P(\rho, \varepsilon)$, where ε is the specific internal energy. The density and pressure values in

the tables were usually in logarithmic units, with about 3 – 5 points specified for each order of magnitude.

In the version of the Courant – Isaacson – Rees method with an explicit evaluation of the derivatives P_ρ and P_ε, the obtained results had to be corrected in order to avoid the non-physical values of the parameters. In particular, such a situation was encountered when the internal energy was found to be lower than the energy defined by the 'cold' compression curve. The numerical algorithm in Ref. [21] (see also Refs [37, 38]) was constructed specially for eliminating such drawbacks. The reliability and efficiency of the algorithm were confirmed by the results of simulation of various phenomena induced by a shock wave in metals, obtained by using this algorithm.

Problem 2. Fig. 16 shows the results of numerical analysis of another problem, namely, the effect of a trapezoidal pressure pulse with maximum amplitude 130 kbar and duration 20 ns on a material, and its reflection at the free surface. The pulse was applied to the left of the target (Fig. 16a). A 500-μm-thick aluminium target was chosen, and the discrete spatial mesh width Δx was equal to 1 μm. The solution of this problem is connected with the interpretation of experimental data [35, 36].

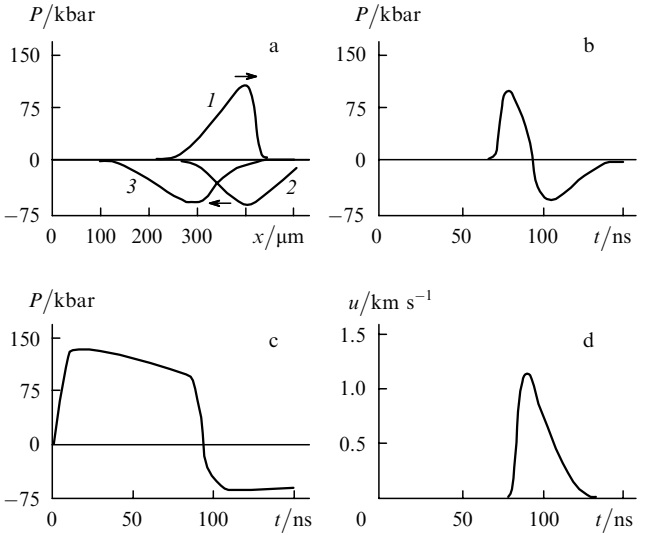

Figure 16. Simulation of pressure pulse propagation and its reflection at the free surface.

Fig. 16a shows the pressure profiles at the instants 70, 120 and 170 ns [curves (*1*), (*2*), and (*3*)] measured from the beginning of the pulse action on the target. The arrows show the direction of pulse propagation in the material of the target. It can be seen that the compression pressure pulse with an initially positive amplitude is transformed into a negative tensile pressure pulse upon reflection at the free surface. Fig. 16b shows the time variation of pressure at a point 60 μm behind the free surface. Experiments reveal a spall at this point, i.e., fracture of the material under the action of tensile pressure following the formation of a transverse crack and flying away of a part of the material in the form of a 'spall plate'. The coefficient of dynamic strength of the material can be estimated from the modulo highest negative tensile pressure obtained in numerical computations at the experimentally observed site of the spallation. Fig. 16c shows the time dependence of the (modulo) maximum pressure over the thickness of the entire target, while Fig. 16d shows the velocity u_{vac} of the free surface of the target as a function of time. Thus, Fig. 16 shows the main features of the phenomena initiated in a material by a relatively weak shock wave, in particular, the transformation of a positive compressive pressure pulse into a negative pulse responsible for the fracture of the target material. A successful simulation of these processes led to physically significant results described in the previous sections.

Problem 3. Fig. 17 shows the results of calculations of the parameters of processes associated with the generation of a shock wave upon collision of a 10-μm-thick aluminium striker flying at a velocity of 4 km s^{-1} with a 100-μm-thick aluminium plate. The spatial mesh width Δx in calculations was put equal to 0.5 μm. Fig. 17a shows the profiles of pressure in a shock wave at the instant 4.96 ns [curve (*1*)] and maximum pressure in the target [curve (*2*)]. Fig. 17b shows the time dependence of pressure for points $x = 0$ and 80 μm [curves (*1*) and (*2*)], maximum pressure over the entire thickness of the target [curve (*3*)] and of the velocity of free surface of the target [curve (*4*)]. The formulation of the problem is associated with the conducted experiments. Numerical calculations make it possible to determine the impact velocity from the time of emergence of shock wave at the free surface [36].

Problem 4. Fig. 18 shows the schematic diagram of the physical experiments on the measurement of heating of the material behind the front of a high-intensity shock wave induced by laser irradiation [7 – 9, 22, 23] (the first publications appeared in the form of Refs [55 – 59]). In this case, a high-intensity shock wave propagates in a metal (Fig. 18a)

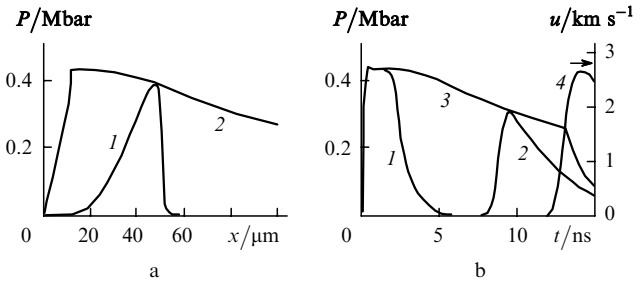

Figure 17. Pressure and velocity distribution upon collision of a striker with an aluminium target.

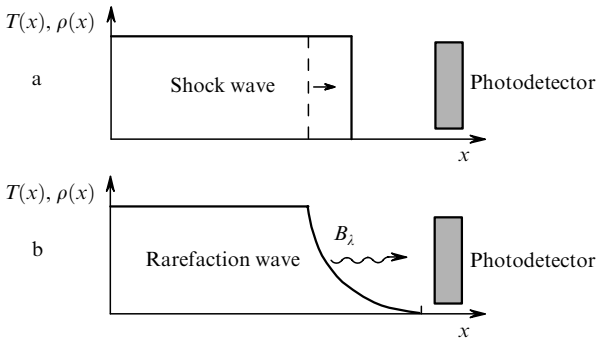

Figure 18. Scheme for measuring emission of the metal surface at various stages of shock-wave propagation through the target.

and then emerges at the free surface (target – vacuum interface), inducing a glow of metal plasma in the resulting expansion wave (Fig. 18b). The glow is measured by photodetectors simultaneously for different wavelengths λ, usually in the 'red' and 'blue' spectral ranges [see Eqns (6) and (7)]. Measurements make it possible to determine the temperature and pressure behind the shock-wave front [8, 9]. Such measurements impose certain constraints on the uniformity and one-dimensionality of the hydrodynamic flows under consideration. Direct measurements of the plasma temperature in a shock wave constitute a complex experimental problem since thermal radiation from hot plasma is shielded and absorbed by cold metal vapour in the rarefaction wave formed as a result of emergence of the shock wave at the free surface [14]. The experimentally measured time variation of the glow temperature of the metal surface was compared with the numerically obtained dependence.

Numerical calculation of the time profiles of the integrated temperature was carried out by solving the time-dependent one-dimensional gas-dynamic equations and by computing the profiles of density ρ and temperature T at various instants of metal unloading in vacuum (Fig. 18b). The obtained density and temperature profiles were then used to determine the total spectral emission brightness over the entire thickness of the metal at each wavelength using formula (6) and taking into account the appropriate absorption coefficients [14].

First such calculations, made for experiments with aluminium, lead and bismuth [22, 23, 59] were based on the exact solution of the wide-range equation of state for each metal in the form of a rarefaction wave. Subsequently, the finite-volume Courant – Isaacson – Rees method was used to determine the parameters of the shock wave generated in aluminium. The computational model used the one-dimensional gas-dynamic equations in Lagrangian coordinates, supplemented by the wide-range semi-empirical equation of state for aluminium [34, 53].

Numerical analysis of such problems requires a high degree of accuracy in the calculation of profiles of gas-dynamic parameters in rarefaction waves in metals. The accuracy of calculations was increased by using special modifications of the numerical method described in [21, 37, 38]. Note that such a modification is essential only for complex equations of state and not for the ideal gas equation.

Thus, the method developed by us for a numerical solution of the equations of hydrodynamics makes it possible to use any equations of state for a substance almost without exception. The numerical codes developed by us proved to be a reliable instrument for calculations using any equations of state and for solution of problems characterised by high gradients of the required quantities.

4.3 Results of numerical calculations of two-dimensional spallation

Consider now the results of numerical solution of some problems in the dynamics of a deformable solid, which were also obtained by using the Courant – Isaacson – Rees method. Non-conservative equations of mechanics of a deformable solid in a movable coordinate system connected with the boundary of the solid were used. The peculiarities of spall in the two-dimensional case for a cylindrical target are shown in Figs 19 – 21 (see also Fig. 10). Fig. 19 shows the experimental setup [2]. The arrows show the direction in

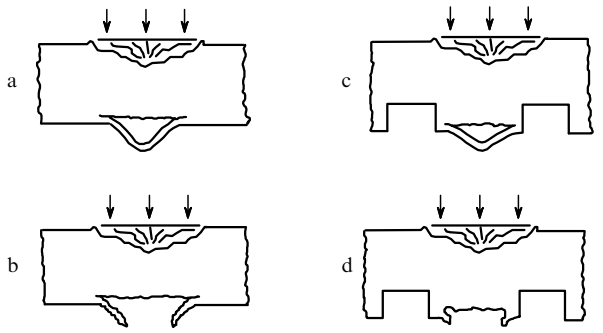

Figure 19. Schematic of laser experiments showing the spall process.

which the laser pulse of intensity about 10^{11} W cm^{-2} acts. Experiments were made on targets without a cut (Figs 19a, b) as well as with a cylindrical cut (Figs 19c, d). Fig. 19 shows the peculiarities of spall in these cases. The spall may be complete (Figs 19b, d) or incomplete (Figs 19a, c). At the initial stage of the process, a cut may facilitate the formation of a cracks along the lateral surface of a protrusion. Hence a complete separation of the spall layer from the target may occur under the same conditions only in the configuration shown in Fig. 19c. In the other configuration (Fig. 19a), a complete spallation is not observed.

Fig. 10 shows the photographs of an aluminium (alloy AMg6M) target with a cut after the spall caused by a laser pulse. The photographs describe various stages of spallation in laser experiments with pulse intensities 3.0×10^{11} (Fig. 10a), 3.5×10^{11} (Fig. 10b), and 4.3×10^{11} W cm^{-2} (Fig. 10c). The resulting ablative pressure is determined by a power law (scaling) [3] [see formula (5)] and is equal to 154, 187 and 247 kbar, while the duration of triangular laser pulses is 40, 10 and 40 ns respectively. The photograph in Fig. 10a corresponds to the case of partial spall (Fig. 19c), while that in Fig. 10c corresponds to complete spall (Fig. 19d).

Figs 20 and 21 show the results of two-dimensional numerical simulation of spallation processes in a target without a cut and with a cut being deformed under the same kind of laser irradiation. Simulation was carried out in a moving cylindrical coordinate system connected with the target boundary. These figures show the isolines of maximum stresses, a larger number of isolines indicating a large stress. Calculations were made using a square mesh with the number of mesh points varying from 40 to 320 along the x axis.

The data presented in Figs 20 and 21 were obtained under the conditions when spallation in experiments occurred only for targets with a cut. The regions in which cracks may appear are hatched in Fig. 21. A vertical crack may appear at the instant $t = 74.3$ ns, while the horizontal one may appear later, at $t = 103.2$ ns. The resulting horizontal crack is superimposed on the vertical crack (not shown in the lowest diagram in Fig. 21). Such cracks have indeed been observed in experiments. In the target shown in Fig. 20, conditions suitable for crack formation are not realised and spall is not observed in these targets (this is confirmed by experiments [2]).

The results presented in Figs 20 and 21 were obtained by V.D. Ivanov and I.B. Petrov of the Moscow Institute of Physics and Technology [60] under a joint project on the

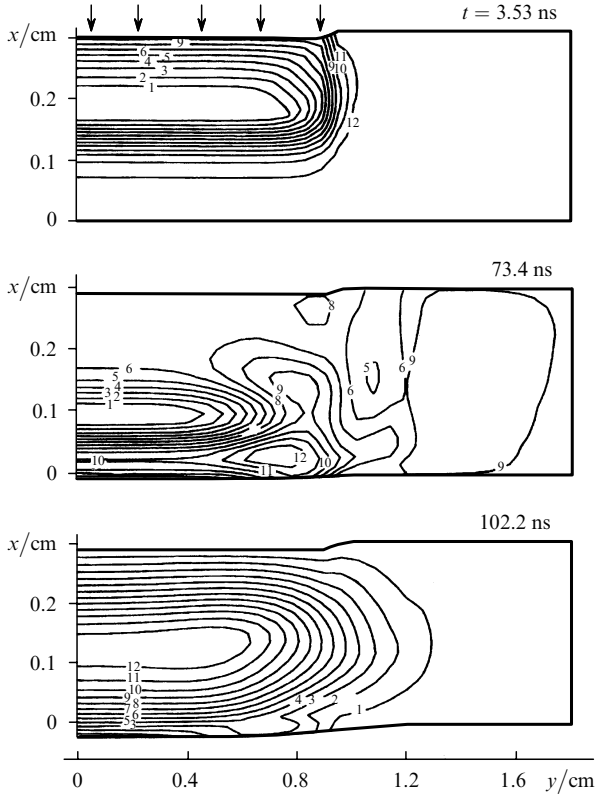

Figure 20. Results of two-dimensional numerical simulation of spallation process for a target without a cut.

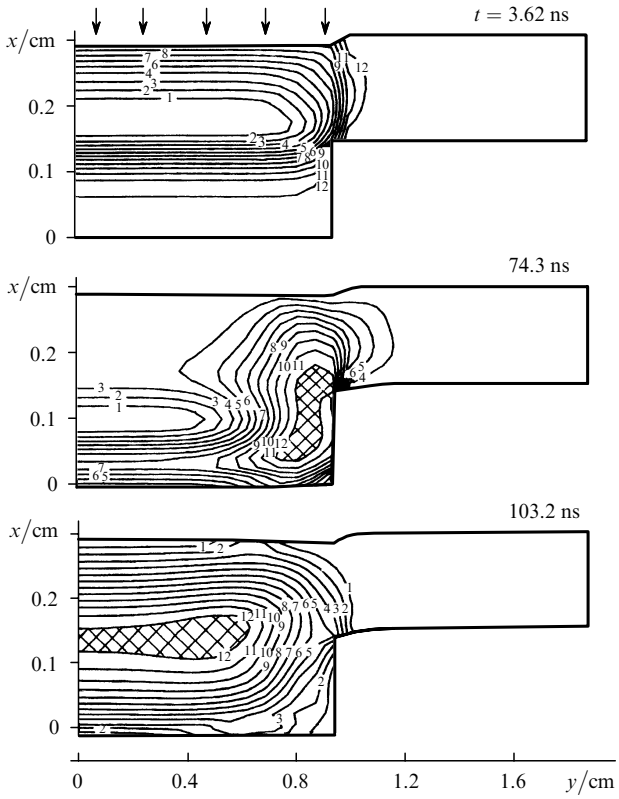

Figure 21. Results of two-dimensional numerical simulation of spallation process for a target with a cut.

theoretical and experimental studies of spallation phenomena with the General Physics Institute, Russian Academy of Sciences. Additional parameters of the spallation process obtained by using numerical simulation in the two-dimensional case are given in Refs [1, 5, 6], the numerical technique used is described in Ref. [60], as well as in Refs [61, 62].

The above examples show that the numerical codes designed and developed by us conform to international standards and can be used successfully for solving important problems associated with the action of high-intensity laser radiation fluxes on matter. Numerical simulation also serves as an important supplement to the experimental methods of investigation at the stage of planning and during measurements, as well as for a correct interpretation of the obtained data.

5. Conclusions

The results of our investigations show that laser generation of shock waves can serve as a prospective method for studying the thermophysical and mechanical properties of matter under extremal conditions.

Recording instruments with a high spatial and time resolution are required for studying the thermophysical properties of matter behind the shock-wave front. Special attention must be paid in this case to the initial state of the target.

In the investigations of the mechanical properties of matter at high deformation rates and for dynamic strength close to the critical values, it is important to study the behaviour of the tensile stresses in the spall plane. While interpreting the obtained results, considerable attention must be paid to the specific nature of the experiments: a shock-wave impact may cause a dynamic hardening of the material being studied.

It has been established that only a complex use of experimental and numerical methods can lead to new information in this field of research. An effective use of the numerical simulation methods based on hydrodynamical equations has been made possible owing to the introduction of real semiempirical wide-range equations of state of the materials under consideration.

Acknowledgements. This work was supported by the Russian Foundation for Basic Research (Grant Nos 94-02-03413, 97-02-16456, 00-02-17873, 00-02-17060 and 03-02-16627).

References

1. Abazekhov M.M., Vovchenko V.I., Kil'pio A.V., Kostin V.V., Kochiev D.G., Krasyuk I.K., Pashinin P.P., Suchkov Yu.A., Fortov V.E. *Preprint of the Institute of High Temperatures, USSR Academy of Sciences*, (1), 282 (Moscow, 1990).
2. Vovchenko V.I., Krasyuk I.K., Semenov A.Yu. *Proceedings of the General Physics Institute, RAS*, **36**, 129 (1992).
3. Vovchenko V.I., Krasyuk I.K., Pashinin P.P., Semenov A.Yu. *Dokl. Ross. Akad. Nauk*, **338** (3), 322 (1994) [*J. of Russian Acad. Sci. Physics-Doklady*, **39** (9), 633 (1994)].
4. Vovchenko V.I., Krasyuk I.K., Pashinin P.P., Semenov A.Yu. *Proc. XII Intern. Conf. on Laser Interaction and Related Plasma Phenomena* (Osaka, Japan, 1995; New York, Woodbury: American Institute of Physics, 1996) Vol. 369, Pt 1, p. 369.
5. Kostin V.V., Krasyuk I.K. *Izv. Ross. Akad. Nauk, Ser. Fiz.*, **61** (7), 1359 (1997).

6. Kostin V.V., Fortov V.E., Krasyuk I.K., Kunizhev B.I., Temrokov A.I. *Teplofiz. Vysok. Temp.*, **35** (6), 962 (1997).
7. Vovchenko V.I., Krasyuk I.K., Pashinin P.P., Semenov A.Yu. In: *Advances in Laser Interaction with Matter and Inertial Fusion* (London: World Scientific Publ., 1997) p. 368.
8. Batani D., Koenig M., Benuzzi A., Krasyuk I.K., Pashinin P.P., Semenov A.Yu., Lomonosov I.V., Fortov V.E. *Plasma Phys. Control. Fusion*, 41 (1), 93 (1999).
9. Batani D., Koenig M., Benuzzi A., Krasyuk I.K., Pashinin P.P., Semenov A.Yu., Lomonosov I.V., Fortov V.E. *Laser and Particle Beams*, **17** (2), 265 (1999).
10. Krasyuk I.K. *Us. Fiz. Nauk*, **169** (10), 1155 (1999).
11. Batani D., Fortov V.E., Kilpio A.V., Krasyuk I.K., Lomonosov I.V., Pashinin P.P., Shashkov E.V., Semenov A.Yu., Vovchenko V.I. *Laser and Particle Beams*, **20** (2), 317 (2002).
12. Batani D., Vovchenko V.I., Kanel' G.I., Kil'pio A.V., Krasyuk I.K., Lomonosov I.V., Pashinin P.P., Semenov A.Yu., Fortov V.E., Shashkov E.V. *Dokl. Ross. Akad. Nauk*, **389** (3), 328 (2003) [*J. of Russian Acad. Sci. Physics-Doklady*, **48** (3), 123 (2003)].
13. Anisimov S.I., Prokhorov A.M., Fortov V.E. *Usp. Fiz. Nauk*, **142** (3), 395 (1984).
14. Zel'dovich Ya.B., Raizer Yu.P. *Fizika udarnykh voln i vysokotemperaturnykh gidrodinamicheskikh yavlenii* (Physics of Shock Waves and High-Temperature Hydrodynamic Phenomena) (New York: Dover, 2002; Moscow: Nauka, 1966).
15. Bushman A.V., Fortov V.E. *Usp. Fiz. Nauk*, **140** (2), 177 (1983).
16. Batani D., Bossi S., Hall T.A., Mahdieh M., Koenig M., Krishman J., Benuzzi A., Lower Th., in *Advances in Laser Interaction with Matter and Inertial Fusion* (London: World Scientific Publ., 1997) p. 409.
17. Hall T.A., Benuzzi A., Batani D., Beretta D., Bossi S., Faral B., Koenig M., Krishnan J., Lower Th., Mahdieh M. *Phys. Rev. E*, **55** (6), R6356 (1997).
18. Bossi S., Hall T.A., Mahdieh M., Batani D., Koenig M., Krishnan J., Benuzzi A., Faral B., Boudenne J.M., Lower Th. *Laser and Particle Beams*, **15** (4), 485 (1997).
19. Koenig M., Faral B., Boudenne J.M., Batani D., Benuzzi A., Bossi S. *Phys. Rev. E*, **50** (5), R3314 (1994).
20. *SESAME Report on the Los Alamos Equation-of-State Library* (Los Alamos, T4 Group LANL, 1983, No. LALP-83-4).
21. Semenov A.Yu. *Zh. Vych. Mat. Mat. Fiz.*, **37** (11), 1376 (1997) [*Comp. Maths Math. Phys.*, **37** (11), 1334 (1997)].
22. Semenov A.Yu., Polishchuk A.Ya., Ternovoi V.Ya., Fortov V.E. *Preprint IOFAN No. 25* (Moscow, 1991).
23. Semenov A.Yu., in *Proc. XII Intern. Conf.* (Osaka, Japan, 1995; New York, Woodbury: American Institute of Physics, 1996) Vol. 369, Pt 1, p. 434.
24. Spitzer L. *Physics of Fully Ionized Gases* (London, 1956; Moscow: Mir, 1965).
25. Lee Y.T., More R.M. *Phys. Fluids*, **27** (5), 1273 (1984).
26. McLean E.A., Gold S.H., Stamper J.A., Whitlock R.R., Griem H.R., Obenshain S.P., Ripin B.H., Bodner S.E., Herbst M.J., Gitomer S.J., Matzen M.K. *Phys. Rev. Lett.*, **45** (15), 1246 (1980).
27. Honrubia J.J., Dezulian R., Batani D., Bossi S., Koenig M., Benuzzi A., Grandjouan N. *Laser and Particle Beams*, **16** (1), 1 (1998).
28. Honrubia J.J., Dezulian R., Batani D., Bossi S., Koenig M., Benuzzi A., Grandjouan N. *Laser and Particle Beams*, **16** (1), 13 (1998).
29. Lower Th., Sigel R., Eidman K., Folders I.B., Huller S., Massen J., Tsakiris G.D., Witkowski S., Preuss W., Nishimura H., Shiraga H., Kato Y., Nakai S., Endo T. *Phys. Rev. Lett.*, **72** (20), 3186 (1994).
30. Evans A.M., Freeman N.J., Graham P., Horsfield C.J., Rothman S.D., Thomas B.R., Tyrrel A.J. *Laser and Particle Beams*, **14** (2), 113 (1996).
31. Anisimov S.I., Imas Ya.A., Romanov G.S., Khodyko Yu.V. *Deistvie izlucheniya bol'shoi moshchnosti na metally* (Action of High-power Radiation on Metals) (Moscow: Nauka, 1970).
32. Grigoriev I.S., Meilikhov E.Z. (Eds) *Handbook of Physical Quantities* (Boca Raton, FL: CRC Press, 1997; Moscow: Energoatomizdat, 1991).
33. Benuzzi A., Koenig M., Faral B., Krishnan J., Pisani F., Batani D., Bossi S., Beretta D., Hall T., Ellwi S., Huller S., Honrubia J., Grandjouan N. *Phys. Plasmas*, **5** (6), 2410 (1998).
34. Bushman A.V., Kanel G.I., Ni A.L., Fortov V.E. *Intense Dynamic Loading of Condensed Matter* (London: Taylor and Francis, 1993; Chernogolovka: Izd. Inst. Khim. Fiz., Akad. Nauk SSSR, 1998).
35. Kil'pio A.V., Kochiev D.G., Malyutin A.A., Pashinin P.P., Suchkov Yu.A., Shashkov E.V. *Proceedings of the General Physics Institute, RAS*, **36**, 202 (1992).
36. Vovchenko V.I., Krasyuk I.K. Pashinin P.P., Prokhorov A.M., Semenov A.Yu., Fortov V.E. *Proceedings of the General Physics Institute, RAS*, **36**, 5 (1992).
37. Kulikovskii A.G., Pogorelov N.V., Semenov A.Yu. *Matematicheskie voprosy chislennogo resheniya giperbolicheskikh system uravnenii* (Mathematical Problems of Numerical Solution of Hyperbolic Systems of Equations) (Moscow: Fizmatlit, 2001).
38. Kulikovskii A.G., Pogorelov N.V., Semenov A.Yu. *Mathematical Aspects of Numerical Solution of Hyperbolic Systems. Monographs and Surveys in Pure and Applied Mathematics. V. 118* (Boca Raton, FL: Chapman & Hall/CRC, 2001).
39. Kanel' G.I., Razorenov S.V., Utkin A.V., Fortov V.E. *Udarnovolnovye yavleniya v kondensirovannykh sredakh* (Shock-wave Phenomena in Condensed Media) (Moscow: Yanus-K, 1996).
40. Kanel' G.I., Fortov V.E. *Usp. Mekh.*, **10** (3), 3 (1987).
41. Kanel' G.I., Razorenov S.V., Utkin A.V., Fortov V.E. *Izv. RAN, Ser. Mekh. Tverd. Tela* (5), 173 (1999).
42. von Neumann J., Richtmyer R.D. *J. Appl. Phys.*, **21** (3), 232 (1950).
43. Samarskii A.A., Popov Yu.P. *Raznostnie metody resheniya zadach gazovoi dinamiki* (Difference Methods for Solving Gassdynamic Problems) (Moscow: Nauka, 1992).
44. Latter R. *J. Appl. Phys.*, **26** (8), 954 (1955).
45. Boris P.J., Book L.D. *J. Comput. Phys.*, **11** (1), 38 (1973).
46. Boris P.J., Book L.D., in *Controlled Nuclear Fusion, Ser. Computational Methods in Physics* (New York: Academic Press, 1976; Moscow: Mir, 1980).
47. Godunov S.K. *Usp. Mat. Nauk*, **12**, No. 1 (73), 176 (1957).
48. Godunov S.K. *Mat. Sbor.*, **47 (89)** (3), 271 (1959).
49. Godunov S.K., Zabrodin A.V., Ivanov M.Ya., Kraiko A.N., Prokopov G.P. *Chislennoe reshenie mnogomernykh zadach gazovoi dinamiki* (Numerical Solution of Gasdynamic Problems) (Moscow: Nauka, 1976).
50. Roe P.L. *J. Comput. Phys.*, **43** (2), 357 (1981).
51. Roe P.L. *Annu. Rev. Fluid Mech.*, **18**, 337 (1986).
52. Courant R., Isaacson E., Rees M. *Commun. Pure Appl. Math.*, **5** (3), 243 (1952).
53. Bushman A.V., Lomonosov I.V., Fortov V.E. *Uravneniya sostoyaniya metallov pri vysokikh plotnostyakh energii* (Equations of States of Metals under High Energy Densities) (Chernogolovka: Izd. Inst. Khim. Fiz., RAN, 1992).
54. Trainor R.J., Lee Y.T. *Phys. Fluids*, **25** (10), 1898 (1982).
55. Ng A., Parfeniuk D., Da Silva L. *Phys. Rev. Lett.*, **54** (24), 2604 (1985).
56. Ng A., Parfeniuk D., Da Silva L. *Opt. Commun.*, **53** (6), 389 (1985).
57. Ng A., Chin G., Da Silva L., Godwal B.K., Cottet F. *Opt. Commun.*, **72** (5), 297 (1989).
58. Godwal B.K., Ng A., Da Silva L. *Phys. Rev. Lett.*, **144** (1), 26 (1990).
59. Kvitov S.V., Bushman A.V., Kulish M.I., Lomonosov I.V., Polishchuk A.Ya., Semenov A.Yu., Ternovoi V.Ya., Filimonov A.S., Fortov V.E. *Pis'ma Zh. Eksp. Teor. Fiz.*, **53** (7), 338 (1991) [*JETP Letters*, **53** (7), 353 (1991)].
60. Ivanov V.D., Petrov I.B. *Proceedings of the General Physics Institute, RAS*, **36**, 247 (1992).
61. Ivanov V.D., Kondaurov V.I., Petrov I.B., Kholodov A.S. *Matem. Model.*, **2** (11), 11 (1990).
62. Magomedov K.M., Kholodov A.S. *Setochno-kharakteristicheskie chislennie metody* (Mesh-characteristic Numerical Methods) (Moscow: Nauka, 1988).